Observations of the chemical and thermal response of 'ring rain' on Saturn's ionosphere

Article

Accepted Version

O'Donoghue, J. ORCID: https://orcid.org/0000-0002-4218-1191, Moore, L., Connerney, J., Melin, H., Stallard, T. S., Miller, S. and Baines, K. H. (2019) Observations of the chemical and thermal response of 'ring rain' on Saturn's ionosphere. Icarus, 322. pp. 251-260. ISSN 0019-1035 doi: 10.1016/j.icarus.2018.10.027 Available at https://centaur.reading.ac.uk/120084/

To link to this article DOI: http://dx.doi.org/10.1016/j.icarus.2018.10.027

Publisher: Elsevier

Observations of the chemical and thermal response of ‘ring rain’ on Saturn’s ionosphere

James O’Donoghue[a], Luke Moore[b], Jack Connerney[c,a], Henrik Melin[d], Tom Stallard[d], Steve Miller[e], Kevin H. Baines[f]

[a] *Planetary Magnetospheres Laboratory, NASA Goddard Space Flight Center, Greenbelt, Maryland, USA*
[b] *Center for Space Physics, Boston University, Massachusetts, USA*
[c] *Space Research Corporation, Annapolis, Maryland, USA*
[d] *Department of Physics and Astronomy, University of Leicester, Leicester, UK*
[e] *Atmospheric Physics Laboratory, Department of Physics and Astronomy, University College London, London, WC1E 6BT, UK*
[f] *NASA Jet Propulsion Laboratory, M/S 183-601, 4800 Oak Grove Drive, Pasadena, CA 91109, USA*

Abstract

In this study we performed a new analysis of ground-based observations that were taken on 17 April 2011 using the 10-metre Keck telescope on Mauna Kea, Hawaii. Emissions from H_3^+, a major ion in Saturn’s ionosphere, were previously analyzed from these observations, indicating that peaks in emission at specific latitudes were consistent with an influx of charged water products from the rings known as ‘ring rain’. Subsequent modeling showed that these peaks in emission are best explained by an increase in H_3^+ density, rather than in column-averaged H_3^+ temperatures, as a local reduction in electron density (due to charge exchange with water) lengthens the lifetime of H_3^+. However, what has been missing until now is a direct derivation of the H_3^+ parameters temperature, density and radiative cooling rates, which are required to confirm and expand on existing models and theory. Here we present measurements of these H_3^+ parameters for the first time in the non-auroral regions of Saturn, using two H_3^+ lines, Q(1,0$^-$) and R(2,2). We confirm that H_3^+ density is enhanced near the expected ‘ring rain’ planetocentric latitudes near 45°N and 39°S. A low H_3^+ density near 31°S, an expected prodigious source of water, may indicate that the rings are ‘overflowing’ material into the planet such that H_3^+ destruction by charge-exchange with incoming neutrals outweighs its lengthened lifetime due to the aforementioned reduction in electron density. Derived H_3^+ temperatures were low while the density was high at 39°S, potentially indicating that the ionosphere is most affected by ring rain in the deep ionosphere. Saturn's moon Enceladus, a known water source, is connected with a dense region of H_3^+ centered on 62°S, perhaps indicating that charged water from Enceladus is draining into Saturn's southern mid-latitudes. We estimated the water product influx using previous modeling results, finding that 432 - 2870 kg s^{-1} of water delivered to Saturn's mid-latitudes is sufficient to explain the observed H_3^+ densities. When considering this mechanism alone, Saturn will lose its rings in 292^{+818}_{-124} million years.

Keywords: Saturn, ionosphere, rings, magnetosphere, ring rain

---

1. Introduction

In the Saturn system, submicrometre charged icy grains are able to stream from the rings into the planetary atmosphere via the magnetic field. This process, termed "ring rain", erodes and sculpts the ring system through the interplay between electromagnetic, gravitational and centrifugal forces (Northrop and Hill, 1982; Connerney, 2013). Saturn's atmosphere adopts this discarded ring matter, causing dramatic changes in ionospheric chemistry and the removal of haze (O'Donoghue et al., 2013; Connerney, 1986). Saturn's ring system is comprised of clusters of ice ranging in size from below 0.01 cm and up to 10 m distributed in an approximately inverse cubic power-law manner, such that the majority of ring system is composed of small fragments (Zebker et al., 1985; Cuzzi et al., 2009). The chemical composition of the rings is considered to be almost pure water ice, but they are thought to be contaminated by tholins - a mixture of simple hydrocarbons (e.g. CH_4 and C_2H_6), nitrogen and other components, giving the rings their characteristic tan color (Nicholson et al., 2008; Cuzzi et al., 2018). Submicrometre-sized ice particles or icy grains are able to acquire charge via photoionization or exposure to a micrometeorite impact's dense plasma cloud (Connerney, 2013). On becoming charged, these grains have an array of velocities with respect to the planetary magnetic field which permeates the rings: this is either faster (super-rotating), slower (sub-corotating) or the same velocity as the moving magnetic field lines, which rotate at the solid-body planetary rotation rate.

Three major forces act on the charged grains in Saturn's rings **along** a given magnetic field line: gravity pulling the grains towards the planet, and the centrifugal and magnetic mirror forces which act to pull the grains back into the ring plane. At 1.62 R_S (where 1 R_S is Saturn's equatorial radius 60,268 km) within the ring plane, charged grains that are stationary with respect to the magnetic field experience only gravitational and centrifugal forces, which are in balance at this location (the grain is stable) (Northrop and Hill, 1982). At radial distances slightly less than 1.62 R_S, however, gravity begins to dominate, accelerating charged grains towards the planet (the grain is unstable) (Northrop and Hill, 1983). However, charged grains moving at Keplerian velocity super-rotate with respect to the magnetic field and therefore orbit magnetic field lines due to the Lorentz force. These grains, unlike those at 1.62 R_S, are subjected to a magnetic mirror force which repels them back towards the ring plane when they approach the planet; this breed of grain therefore has a radius of force balance that is closer to Saturn, which is calculated to be 1.525 R_S (Northrop and Hill, 1983; Northrop and Connerney, 1987; Connerney, 2013). The sharp density gradient between the B and C rings is near 1.525 R_S, and may even be the result of 'ring rain' electromagnetically eroding the rings at this location (Northrop and Connerney, 1987).

Saturn's magnetic dip equator lies above the ring plane offset towards Saturn's north pole, so that near to the ring plane the magnetic field has a component pointing towards the southern hemisphere. As a result, at radial distances $<$1.525 R_S, recently produced ionized grains that are relatively motionless compared to the rings will be drawn southwards; gravitational forces acting parallel to magnetic field lines are in control here. Note that the grains also have a perpendicular (to the ring plane) velocity distribution of their own which pushes them either northwards or southwards; assuming this is a Maxwellian-like distribution, the grains will still preferentially be drawn southwards, with only the highest velocity grains potentially able to escape northwards. Charged grains produced between 1.525 R_S and 1.62 R_S also fall preferentially to the south, but the grains are able to oscillate about the ring plane here due to the weaker gravitational force pulling the grains planetward along field lines (Connerney, 1986). Pathways for an influx of ring material into the equatorial ionosphere have also been modeled. For example, collisional drag may explain the influx of neutral grains (Mitchell et al., 2018), whereas positively charged dust grains are also expected to be deposited near Saturn's equator (Liu and Ip, 2014; Hsu et al., 2018). Such influxes, which have now been observed by Cassini (Mitchell et al., 2018; Perry et al., 2018; Hsu et al., 2018; Waite et al., 2018), would help to explain the observed depletion in ionospheric electron density there (Kliore et al., 2014). Estimating the mass loss of the rings is of great importance for determining the age, lifetime and evolution of the rings, which are presently understood to have existed for between 4.4 million and 4.5 billion years (see Northrop and Connerney, 1987; Connerney, 2013, and references therein).

The Pioneer 11 spacecraft was the first human made object to fly by Saturn in 1979 (Kliore et al., 1980). Saturn's ionosphere was predicted to have an electron density of around 10^5 cm^{-3}, based on photoionization of atmospheric neutrals (mostly H and H_2) by extreme ultraviolet (EUV) radiation from the Sun (McElroy, 1973; Waite et al., 1979). However, when Kliore et al. (1980) analyzed the attenuation of the Pioneer 11 radio signal, which had traveled through Saturn's ionosphere, the electron density peak was found to be $\sim 10^4$ cm^{-3}, an order of magnitude lower than predicted. Later, the Voyager 1 and 2 spacecraft, in 1980 and 1981 respectively, showed peak electron densities between $\sim$6x10^3 cm^{-3} and $\sim$2.3x10^4 cm^{-3} (Atreya et al., 1984). The lowest electron densities were found at 36° north, while the highest densities were found at 73° north: this was counter-intuitive since the electron production mechanism is solar EUV ionization, which is maximized at mid-to-low latitude, depending on season. These model-observation discrepancies could be resolved however, with the introduction of a planet-wide exogenous water influx of $\sim$4x10^7 molecules cm^{-2} s^{-1}, which leads to a net reduction in electron density (Connerney and Waite, 1984; Moses and Bass, 2000). In addition, a localized water influx of $\sim$2x10^9 molecules cm^{-2} s^{-1} was predicted to fall into Saturn from the inner edge of the B ring (at $\sim$1.525 R_S) (Connerney and Waite, 1984). The Cassini spacecraft later revealed latitudinal variations of peak electron densities using 59 radio occultations, with values ranging from $\sim$1x10^3 cm^{-3} to $\sim$3x10^4 cm^{-3} which correspond to the low-mid latitudes and auroral regions, respectively (Kliore et al., 2014).

Observations consistent with a ring-derived water influx that flows along magnetic field lines were first found using Voyager 2 green filter images of Saturn by Connerney (1986), which showed dark bands (indicating less reflection of sunlight) at 44°, 46°, 52° and 64° planetocentric latitude north. These bands map along magnetic field lines to 1.525 R_S, 1.62 R_S, 1.95 R_S and 3.95 R_S, respectively, in the ring plane. The first two listed radial distances correspond to the theoretical water sources between the B and C rings discussed earlier, while 1.95 R_S corresponds to the Cassini division, and 3.95 R_S is the orbit of Enceladus - a known source of water to the Saturnian magnetosphere (Dougherty et al., 2006; Hansen et al., 2011). The reduction in reflected light leading to these dark bands is thought to indicate the loss of stratospheric haze: Connerney (1986) proposed that haze particles could act as condensation nuclei to the downward diffusing water, thus making haze particles heavy enough to sink. Saturn's hydrocarbon (e.g. C_2H_2) abundance was calculated at four latitudes using Hubble Space Telescope (HST) observations, with a minimum value found at 41° south while increasing towards the polar regions (Prangé et al., 2006). As photochemical models show that the presence of water in the stratosphere depletes hydrocarbons (Moses and Bass, 2000), the results were described by Prangé et al. (2006) to be consistent with an influx of water flowing from the rings to the atmosphere via magnetic field lines.

H_3^+, one of the most abundant ions in Saturn's ionosphere, is produced in the following reaction chain:

$$\begin{aligned}
H_2 + e^* &\rightarrow H_2^+ + e + e && \text{Impact ionization (aurorae),} && (1)\\
H_2 + \text{EUV} &\rightarrow H_2^+ + e && \text{Photoionization (sunlight),} && (2)\\
H^+ + H_2(v{\geq}4) &\rightarrow H_2^+ + H && \text{Vibrationally excited } H_2\text{,} && (3)\\
H_2^+ + H_2 &\rightarrow H_3^+ + H && \text{Proton-hopping reaction.} && (4)
\end{aligned}$$

Where e^* is a fast electron and EUV is an extreme ultraviolet photon from the Sun. As soon as H_2^+ is created by reactions (1) - (3), reaction (4) takes place almost instanteously (Miller et al., 2010; Stallard et al., 2015). In the auroral/polar region, H_3^+ peaks in density at an altitude of ~1155 km above the 1-bar pressure surface (Stallard et al., 2012), and production occurs in the range 900 to 4000 km (Tao et al., 2011).

In 2011, the 10 meter Keck II telescope on Mauna Kea, Hawaii, was used to observe the pole-to-pole H_3^+ ion emissions from Saturn (O'Donoghue et al., 2013). Broad peaks in H_3^+ intensity were discovered at planetocentric latitudes 43° and 38° north and south, respectively. As a result of the geometry of Saturn's magnetic field, which can be thought of as being approximated by a dipole that is slightly offset north of the planet's center, both latitudes share a common field line; this field line intersects the ring plane at ~1.525

R_S (Connerney, 1986). Magnetic conjugacy was directly observed, so the intensity peaks that were found are related to the magnetosphere. Following this observation, Moore et al. (2015) demonstrated through modeling that the increase in H_3^+ emissions was better explained via an increase in H_3^+ density, rather than a (column-averaged) H_3^+ temperature increase. It was found that any water product inflow under $1x10^7$ molecules cm^{-2} s^{-1} will rapidly recombine with electrons, mitigating the loss of H_3^+ by the same process, such that H_3^+ densities ought to be larger where water falls. However, Moore et al. (2015) also found that for large water influxes (greater than $\sim 2x10^8$ molecules cm^{-2} s^{-1}) the loss rate of H_3^+ by charge-exchange with water begins to overtake the enhancement in H_3^+ by the reduction in electron density.

More recently, the signature of ring rain in H_3^+ emissions were re-detected in Keck II telescope observations taken in 2013; the brightness of these emissions was a factor of $\sim$4 lower than in 2011, likely owing to an estimated 90 K decrease in ionospheric temperature from 2011 to 2013 (O'Donoghue et al., 2017). Surprisingly however, the contrast between bright and dim features in H_3^+ emissions were larger in 2013, indicating an increased influx of ring material. Indeed, because the opening angle of the rings was larger in 2013, more of the ring's surface area is exposed to solar EUV ionization, so the production of charged icy grains ought to be larger (O'Donoghue et al., 2017). In 2017 the Cassini spacecraft flew between the planet and rings, allowing for the first time the ability to probe the ring-planet interface region in situ. Onboard Cassini, the impact mass spectrometer Cosmic Dust Analyzer (CDA; Srama et al. (2004)), detected the presence of grains tens of nanometers in size at high concentration near the ring plane and at mid-latitudes in the northern and southern hemispheres: a spectacular confirmation of the ring rain process (Hsu et al., 2018). In the present paper we continue to expand our understanding of ring-atmosphere coupling by assessing the thermal and chemical influence ring rain has on Saturn's ionosphere for the first time, through a new analysis of Keck II data taken in 2011 (O'Donoghue et al., 2013).

2. Observations and data reduction

Ground-based observations of Saturn were obtained on 17 April 2011, between 10:33:42 and 12:46:28 Universal Time (UT), using the 10-metre Keck telescope on Mauna Kea, Hawaii. The dataset obtained in this observation is available in the linked Research data. Saturn's northern hemisphere was tilted towards the Earth (and the Sun) with a sub-Earth latitude of 8.2° - Saturn was in northern spring. The collected light was passed to the high-resolution Near-InfraRed SPECtrometer, NIRSPEC (McLean et al., 1998), which was used in cross-dispersed mode with a resolution of R = $\lambda/\Delta\lambda$ ~25,000, providing a spectral resolution of $\Delta\lambda \approx 1.59 \times 10^{-4}$ μm at 3.975 μm. The wavelengths covered were near 3.5 and 4.0 μm, as they include the Q- and R-Branch ro-vibrational transition lines of the H_3^+ ion. NIRSPEC's slit dimensions were configured to be 0.432″ wide by 24″ long, with a pixel on the CCD corresponding to 0.144″ squared on the sky. The spectrometer slit was aligned along Saturn's noon meridian in a north-south direction, along the axis of the planet's rotation as shown in Figure 1. Note that Saturn's magnetic field is co-aligned with the planetary axis of rotation to 0.0095° (Dougherty et al., 2018). While the planet rotated, spectral images were acquired of Saturn between 103 - 176° Saturn System III Central Meridian Longitude (CML). Each set of spectra acquired consists of twelve 5-s integrations, creating exposures 60 s long, consisting of Saturn (A) and sky (B) frames with the telescope slewing between the relevant positions of each in the sky in an ABBA pattern: in total, 46 A and 46 B frames were captured.

Standard astronomical data reduction techniques were applied to the data, such as sky subtraction, accounting for non-uniformity in the response of NIRSPEC's detector and flux calibration (using the star HR 6035). These processes ensure that unwanted emissions from Earth's atmosphere (mainly from water), telescope and instruments are removed, and that photon counts at the detector are converted to units of physical flux - see e.g. O'Donoghue et al. (2016) for more details. After data reduction, each spectral image is aligned before being co-added to produce a single image representing the entire dataset, selected wavelengths of which are shown in Figure 2. Using geometric information obtained from planetary ephemeris (NASA's Horizons web interface at https://ssd.jpl.nasa.gov/horizons.cgi), planetocentric latitudes were assigned to the data. Telluric seeing, which during this period was ~0.4″, adds uncertainty in determining the location of the planet's limbs since the data are spatially smeared by ±2 pixels, equating to ~2 of latitude near 45° north. A cosine correction of the planetary emission angle was applied to remove the line-of-sight effects of viewing geometry.

One of the challenges of this work is measuring H_3^+ transition line emissions at mid-to-low latitudes, which are up to an order of magnitude weaker

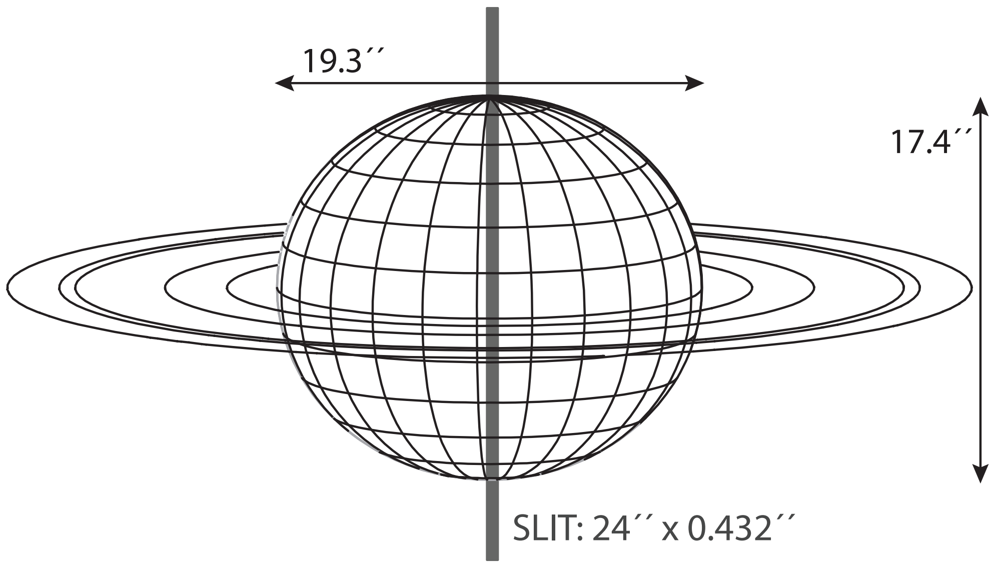

Figure 1: Saturn in conditions of northern spring, 17 April 2011. Gridlines on the planetary body are spaced in 15-degree intervals of longitude and latitude. The arrowed lines show the angular extent of Saturn and the dimensions of the NIRSPEC spectral slit in seconds of arc. This image was generated using the Planetary Data System (PDS) online tools at https://pds-rings.seti.org/tools/.

than auroral/polar emissions at Saturn. H_3^+ emissions are therefore more sensitive to residual signals left over from the data reduction process, e.g. sky emission subtraction leaves residuals of about 1% of the peak auroral intensity, which is about 1-10% of the peak intensity at mid-to-low latitudes. This is mitigated against by selecting larger spatial areas (longitude and latitude) in order to increase the signal to noise. The next challenge is in how to deal with unwanted emissions emanating from Saturn itself, which has at least over 100 different species of neutrals and ions present (Moses and Bass, 2000); the emissions wavelengths from many of the lower-abundance members of these species are not fully understood, and so may register as localized noise at specific wavelengths and latitudes. The two H_3^+ lines in this study, however, were chosen in Kronian-atmospheric windows produced by methane's absorption of sunlight, avoiding noisy regions at most latitude seen on the left of panel b) in Figure 2. Previous studies have been successful in deriving H_3^+ temperatures and densities from two H_3^+ spectral lines (O'Donoghue et al., 2016; Johnson et al., 2018). Figure 3 shows the co-addition of data from Figure 2 between 30° to 39° planetocentric latitude

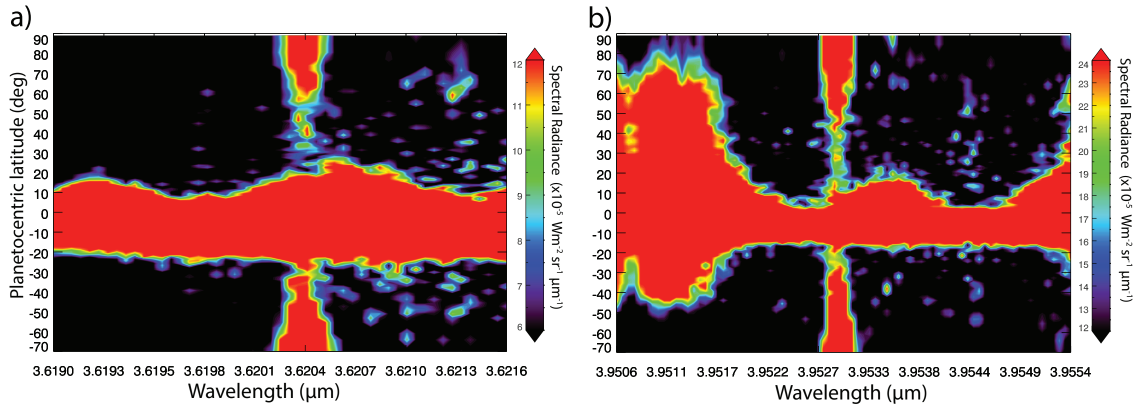

Figure 2: Fully reduced co-added spectrum composed of 46 spectral images of Saturn, in wavelength and planetocentric latitude. These two panels are centered on two (vertical) ro-vibrational transition lines of H_3^+. In a) is the R-branch H_3^+ transition line designated R(2,2$^-$), while b) shows the fundamental H_3^+ line, Q(1,0$^-$). Both lines are observable because methane absorbs most of the incident solar radiation in these wavelength ranges. The horizontal emissions near the equator are the continuum reflection of sunlight from the rings. Note that the spectral radiance is 'thresholded' between the numbers shown in the color bars.

south. Fitting to H_3^+ lines (described in the Data Analysis section) requires that the minimum background spectral radiance is found and subtracted, so that the H_3^+ line begins from a background of zero. Pixel-to-pixel extremes, such as hot pixels that survived the data reduction process, were accounted for by smoothing the data by 0.0025 μm (4 pixels) prior to establishing the minima of each bin. Figure 3 displays a background subtraction as shifted data (black asterisks), with the pre-shifted data in grey.

To remove unwanted, blended emissions from the H_3^+ lines (shown in red in Figure 3 and labeled as noise), a non-linear least squares curve fitting routine called MPFIT was employed (Markwardt, 2009). In this work, MPFIT is programmed to look for multiple Gaussians within the data; the first Gaussian distribution is fixed in wavelength to an H_3^+ line and allowed to vary in height and width, while additional Gaussians are used to characterize nearby noise and are free to vary in wavelength, height and width. Typically each H_3^+ line is either not blended or is blended with one other line, as is the case in Figure 3). Once a solution is found, the Gaussian noise distributions are subtracted from the data, leading to the gold colored H_3^+-only line in Figure

3.

Standard deviations in the Q-and R- branch data were calculated from the wavelength ranges 3.954 - 3.955 μm and 3.618 - 3.62 μm, respectively, and included the planetocentric latitude range 40° to 90°N. These areas were chosen to represent the standard deviation, rather than the area immediately around the H_3^+ lines, in order to accurately represent the dispersion of data in the array: the standard deviation is thus less affected by small spatial/spectral scale features, such as residuals leftover from sky subtraction and uncharacterized emissions from Saturn's many species. When estimating the minimum background of the smoothed array for the purposes of shifting the array down, an additional uncertainty is introduced: this is included by calculating the standard deviation of the smoothed array in the latitude and wavelength ranges above. A final uncertainty is introduced after using MP-FIT - the model-data difference known as residuals. These residuals, along with the standard deviations above, are propagated through to achieve the final standard deviations shown in Figure 3. Note that the Q-branch data are a factor ∼3 brighter than the R-branch, so three standard deviations are shown in this figure instead of one for aesthetic purposes.

3. Data analysis

H_3^+ emits a spectrum of at least 3 million ro-vibrational transition lines, and each line varies in intensity at a particular rate that depends on the ion's temperature (Neale et al., 1996). With a model of this temperature dependence we can therefore obtain the column-averaged H_3^+ temperature, $T_{H_3^+}$ (Kelvin), through observations of the ratio between two or more H_3^+ emission lines. The model fitting routine used herein uses the spectroscopic line list from Neale et al. (1996), the latest H_3^+ partition function constants from Miller et al. (2010), and varies a sum of Gaussian distributions that represent H_3^+ (called the spectral function) until the line-ratios match the least squares fit to the observed data (for more detail see Melin et al., 2013, and references therein). To find the total number of emitting ions per unit area - the H_3^+ column density - we divide the observed emissions by those that a single H_3^+ ion emits at the temperature calculated above. This produces a column-integrated density, $N_{H_3^+}$ (cm^{-2}). The radiative cooling rate (or, radiance) of H_3^+ is given by $L_{H_3^+}$ (Wm^{-2} sr^{-1}): it is the radiative power imparted by H_3^+ at all wavelengths from a surface area to a given steradian

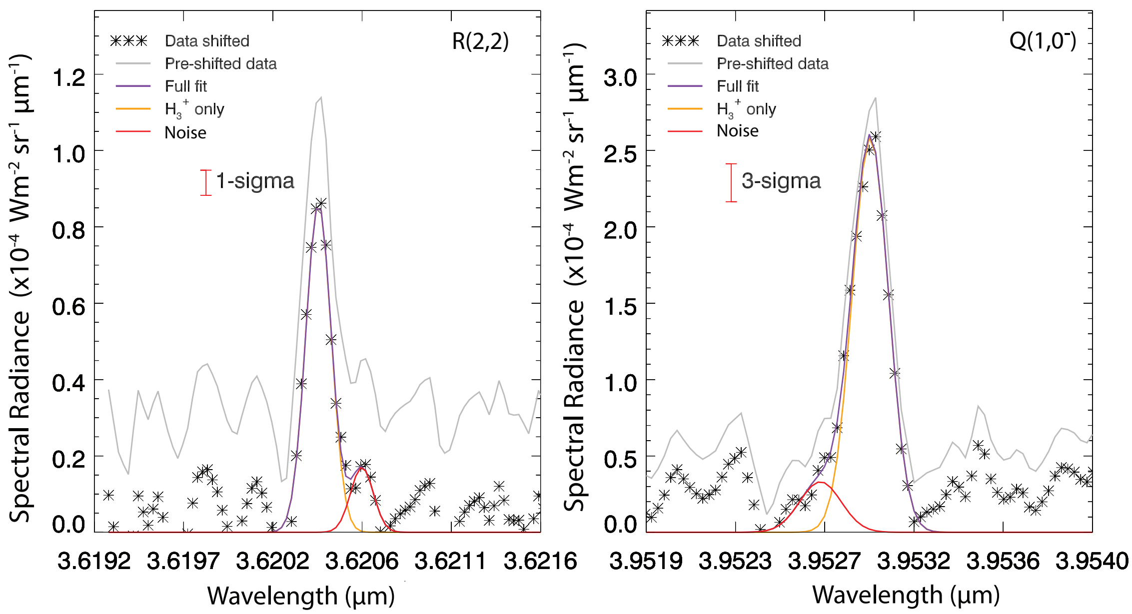

Figure 3: Spectral radiance of Saturn co-added from 103 - 176° CML and 37 - 47°S planetocentric latitude, extracted from the data presented in Figure 2. A full description of the features of this figure is given in the main text.

of solid angle. Calculation of $L_{H_3^+}$ is achieved by multiplying $N_{H_3^+}$ by the sum of all emissions of a single H_3^+ ion for the calculated $T_{H_3^+}$. The radiative cooling rate was introduced by Lam et al. (1997) as 'total emission' in a study of Jupiter's ionospheric H_3^+. $L_{H_3^+}$ is a useful parameter as it reveals the amount of energy lost by the ionosphere via radiative cooling to space by H_3^+.

Prior to fitting to data using the above H_3^+ model, the H_3^+-only emissions and a single standard deviation from Figure 3 are extracted. In Figure 4, modified H_3^+-only line emissions from Figure 3 are shown, with each new data curve representing an original H_3^+-only curve, but with the addition and subtraction of one standard deviation from each respective panel. The H_3^+-fitting model is then run as follows: first, the lower data curve from panel a) is fitted alongside the higher data curve in panel b) and second, the higher data curve from panel a) is fitted with the lower data curve of panel b). Performing the fits this way ensures that the full range of possible line ratios between these two H_3^+ lines are included in the results, based on the relative standard deviations from each panel. Having a range of possible fits leads to a range of H_3^+ parameter outputs ($T_{H_3^+}$, $N_{H_3^+}$, $L_{H_3^+}$): the upper and lower values for each parameter, along with the uncertainties from the model fitting itself, represent the overall uncertainties in the results to follow. Note that the data in Figure 4 rests on random noise that was generated within the bounds of one standard deviation, and that this used to illustrate the uncertainty in background of the array.

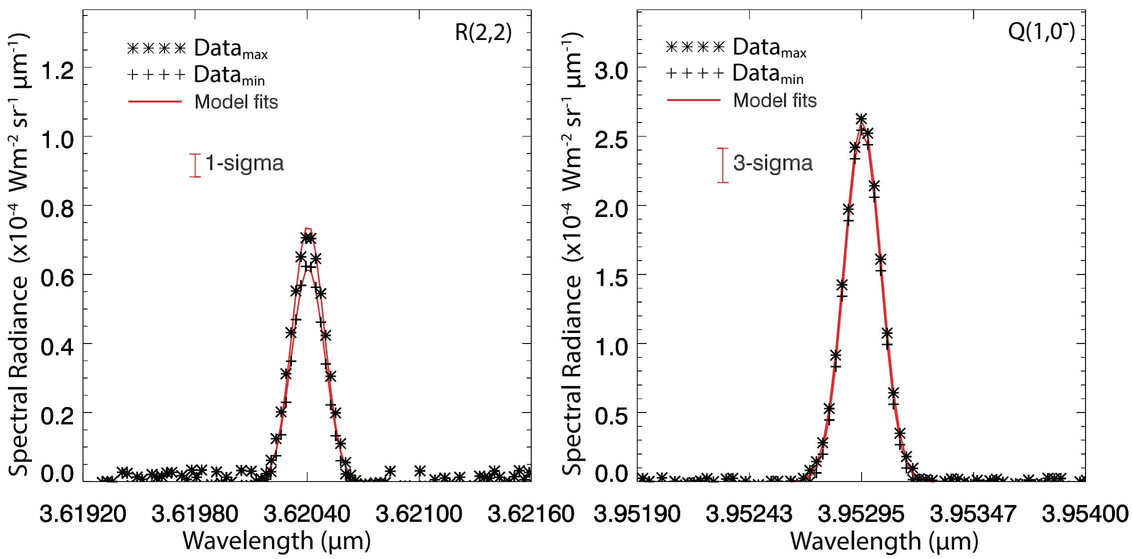

Figure 4: As Figure 3, but only including a modified version of H_3^+-only emissions and model fits to the data, as described in the main text.

In order to map planetary latitudes to radial distance in the ring plane, the path of magnetic field lines are traced from the ionosphere to the ring plane using a model of Saturn's magnetosphere. For this, we use the Voyager 2 "Z3" magnetic mapping model of Connerney et al. (1982) with the coefficients: g1 = 21,248 nT, g2 = 1,613, g3 = 2683 (Dougherty et al., 2005). Here we used spherical harmonic coefficients based on Voyager 2 spacecraft derived data. This model includes a full order-3 internal field, ring current and accounts for the oblateness of the planet, and uses a Saturn equatorial radius of 60,268 km. An ionospheric height of 1200 km was chosen for this mapping, which is approximately the observed H_3^+ density peak altitude (Stallard et al., 2012), and is consistent with modeled H_3^+ altitudes at mid-latitude (Kim et al., 2014).

4. Results and discussion

Owing to this dataset having the highest signal strength of H_3^+ recorded at mid latitudes on Saturn, we are able to see and use two spectral lines to calculate column-averaged H_3^+ temperatures, densities and radiative cooling rates, allowing us to finally measure how ring rain affects upper-atmospheric chemistry and energy balance. In Table 1 we present the results obtained by fitting to Saturn's local-noon H_3^+ emissions, integrated between 103 - 176° CML. A total of eleven fits were obtained from pole to pole, with an absence of fits near the equator being due to a combination of low H_3^+ signal to noise and interference from the continuum reflection of sunlight by the rings. These results are the first non-auroral (<70°N/S latitude) H_3^+ parameters to ever be derived at Saturn, and so offer new insights into the thermal and chemical modification of the ionosphere and co-located thermosphere by the impinging ring rain phenomenon and other phenomena. The following results map mostly to features in the equatorial plane such as the A, B and C subdivisions of the main rings, Saturn's satellite's Mimas and Enceladus, the E-ring and the aurorae. In addition, a B/C ring boundary was also studied due the expectation that it is a source of charged icy grains.

Figure 5 shows $N_{H_3^+}$ and normalized inverse (stratospheric) haze opacity, τ^{-1} taken from Connerney (1986), as a function latitude and radially mapped distance. Connerney (1986) proposed that haze particles could act as condensation nuclei to the downward diffusing water, thus making haze particles heavy enough to sink. Here we show the inverse haze opacity, which represents the degree to which the haze layer has become thinned (by ring rain): a value of 0 means the haze layer is dense, while a value of 1 means the haze is less dense. Densities of H_3^+ are high near Saturn's auroral regions, but reach their highest point near the expected location of a 'ring rain' influx emanating from the B- and C-rings. In the north, the results suggest that the inner-edge of the B-ring is the largest source of icy grains. While the uncertainties are large in the northern hemisphere, limiting our ability to draw definitive conclusions about the influence of rain there, 39°S was found to have a high $N_{H_3^+}$, with uncertainties mostly clear of those at adjacent latitudes. These peaks in $N_{H_3^+}$ most likely indicate that an influx of ring material (such as water) is falling at these latitudes and removes electrons, which in turn increases the

Table 1: Saturn's fitted H_3^+ parameters as a function of planetocentric latitude (Lat PC) and corresponding magnetic field mapping out to the equatorial plane (Eq. Radius). Note that this mapping was evaluated at 1200 km altitude above Saturn's 1-bar pressure surface. Parameter uncertainties shown are one standard deviation. The listed features are the approximate locations covered by each latitudinal swath.

Region	Lat PC	Eq. Radius (R_s)	Feature	$N(H_3^+)$ 10^{11} cm^{-2}	$T(H_3^+)$ Kelvin	$L(H_3^+)$ 10^{-6} Wm^{-2} sr^{-1}
1	80 - 69°N	30.7 - 5.7	Aurora	4.9 ± 3.8	443 ± 65	4.3 ± 0.8
2	69 - 60°N	5.7 - 2.97	Enceladus/E-ring	1.0 ± 0.6	515 ± 58	4.1 ± 0.6
3	60 - 53°N	2.97 - 2.09	A-ring to Mimas	5.3 ± 4.5	424 ± 69	2.6 ± 0.5
4	51 - 43°N	1.93 - 1.51	B-ring	11.6 ± 9.2	377 ± 47	2.4 ± 0.3
5	47 - 43°N	1.69 - 1.51	B/C Boundary	6.1 ± 5.4	433 ± 84	2.8 ± 0.6
6	26 - 37°S	1.25 - 1.52	C-ring	1.1 ± 0.8	544 ± 96	4.6 ± 1.2
7	35 - 44°S	1.46 - 1.81	B/C Boundary	24 ± 16.5	348 ± 31	2.9 ± 0.2
8	37 - 47°S	1.52 - 1.99	B-ring	7.2 ± 4.5	396 ± 36	3.3 ± 0.3
9	47 - 57°S	2.0 - 2.9	A-ring to Mimas	3.5 ± 1.3	455 ± 27	6.5 ± 0.4
10	57 - 67°S	2.9 - 5.8	Enceladus/E-ring	5.2 ± 1.2	479 ± 17	15.5 ± 0.7
11	68 - 75°S	6.4 - 18.0	Aurora	2.7 ± 0.7	519 ± 23	14.4 ± 0.8

H_3^+ density by mitigating the H_3^+-electron recombination rate (Moore et al., 2015). The highest density was observed in the southern hemisphere from region 7, which is expected since the magnetic field permeating the rings is inclined towards the south (Connerney, 1986). The low H_3^+ density of region 6 appears to be the result of an exceptionally high rain influx: we define this area as an 'overflow' region, and it coincides with the thinnest region of stratospheric haze. Indeed, Connerney (1986) predicted an influx near 38° S of $2\text{x}10^9$ molecules cm^{-2} s^{-1} which is in agreement with Moore et al. (2015), who show that influxes greater than $4\text{x}10^8$ molecules cm^{-2} s^{-1} are enough to locally reduce $N_{H_3^+}$ through charge-exchange between H_3^+ and water, which begins to overwhelm the enhancement in H_3^+ given by the reduction in electron density.

The northern regions 4 and 5 have an average column-integrated H_3^+ density of 8.85 ±5.3 $\text{x}10^{11}$ cm^{-2}, which is consistent with a water product influx of between $7\text{x}10^6$ and $7\text{x}10^7$ cm^{-2} s^{-1}, according to Figure 4 of Moore et al. (2015). This implies that regions 4 and 5 deliver 27 ±22 kg s^{-1} of water products to the ionosphere, if the flow is deposited at all longitudes. For regions 7 and 8, the average H_3^+ density of 15.6 ±8.5 $\text{x}10^{11}$ cm^{-2} implies a water product influx of 14±7 kg s^{-1}. To explain the H_3^+ density range of region 6, a water product flow rate of either near $4x10^5$ molecules cm^{-2} s^{-1} or $2x10^9$ molecules cm^{-2} s^{-1} is required (Moore et al., 2015). Since the latter value is what is predicted by Connerney and Waite (1984), we favor the higher rate here and thus eliminate the problem of degeneracy for this region. An influx $6x10^8$ - $4x10^9$ molecules cm^{-2} s^{-1} can explain the density range found in region 6 (Moore et al., 2015), which corresponds to 420 - 2800 kg s^{-1} of water products entering the planet. In total, we estimate an influx of water products from Saturn's rings to the planet, at the latitudes measured here, of 432 - 2870 kg s^{-1}. At this mass loss rate, and using a total mass of Saturn's rings of 1.52 $x10^{19}$ kg (Voosen, 2017), the ring system has 292^{+818}_{-124} million years before it is completely consumed by the planet. This estimate of ring lifetime has a number of assumptions: 1) that the ring system is able to disperse over time (e.g. by micrometeoroid bombardment), allowing the C-ring to act as a continually replenished source region; 2) we measured Saturn during the conditions of northern Spring, so the values above do not yet account for how Saturn's ring rain influx may change with season; 3) equatorial losses were not accounted for here (Perry et al., 2018; Waite et al., 2018), so the mass loss rate and ring lifetime estimates above are upper limits based strictly on a mid-latitude influx of water products alone.

Moore et al. (2015) estimated $N_{H_3^+}$ from the observations of H_3^+ Q(1,0^-) line emission taken by O'Donoghue et al. (2013), i.e. the same observations reported here (e.g. see Figure 2), by assuming a range of $T_{H_3^+}$ of ∼430 - 500 K in both hemispheres. H_3^+ densities near 39°S were modeled to be 1.8 - 3.2 $x10^{11}$ cm^{-2}, while those at 45°N were found to be range 1.6 - 3 $x10^{11}$ cm^{-2} (Moore et al., 2015). By comparison, average densities of 11.6 ± 9.2 $x10^{11}$ cm^{-2} and 24 ± 16.5 $x10^{11}$ cm^{-2} were found near 45°N and 39°S, respectively, were derived from our observations. The northern values are (within uncertainties) in loose agreement with modeling, but the observed southern values exceed the expected density. To explore why this is the case, we examine the fitted values of $T_{H_3^+}$ in Figure 6, which show temperatures of 377 ± 47 K at 45°N and 348 ± 31 K at 39°S. Since the observed intensity of a given H_3^+ line depends linearly upon the ion's density and exponentially on the ion's temperature (Melin et al., 2014), a model of H_3^+ emission that uses an overestimate of temperature will necessarily underestimate the ion's density (and vice versa). The modeled H_3^+ densities will be larger at most latitudes

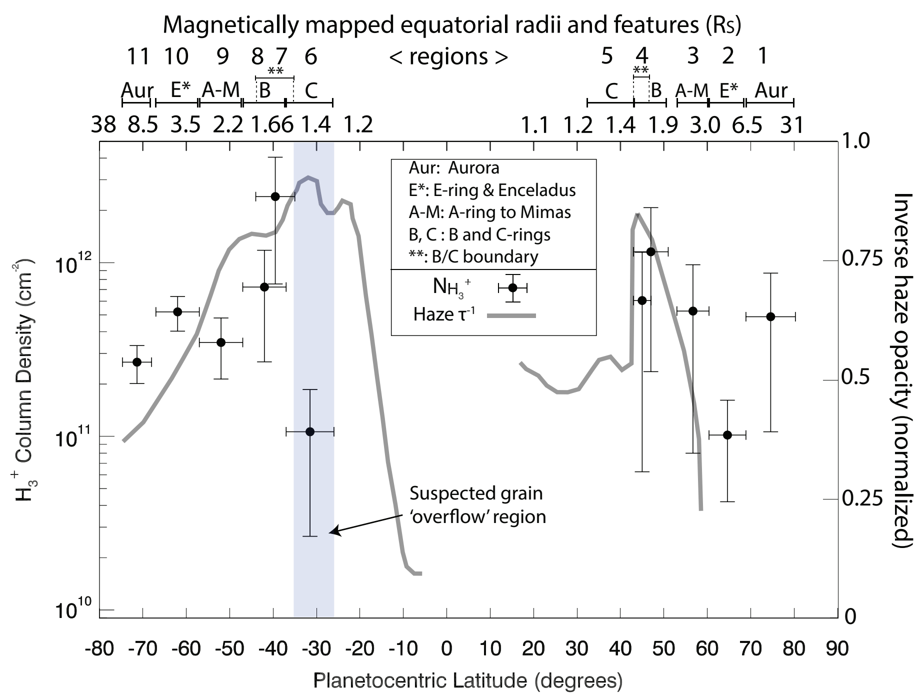

Figure 5: Saturn's fitted H_3^+ column densities, $N_{H_3^+}$ and normalized inverse haze opacity, τ^{-1}, as a function of planetocentric latitude and corresponding magnetic field mapping out to the equatorial plane, R_s. Latitudinal/radial ranges of each measurement are given by the horizontal lines on each value, while the density uncertainties (one standard deviation) are given by vertical lines. A blue-shaded region indicates the 'overflow' region where the largest influx of ring rain is expected (2×10^9 molecules cm^{-2} s^{-1}). The listed features are the approximate locations covered by each latitudinal swath.

in the model of Moore et al. (2015), provided that the observed temperatures of 348 - 377 K are used instead of the previous 430 - 500 K (Luke Moore, personal communication).

We will now consider how the altitudinal distribution of the ring rain influx may give rise to an anti-correlation between $T_{H_3^+}$ and $N_{H_3^+}$ (the Spearman's rank coefficient between these parameters is r = -0.93). At 39°S, for example, ring rain enters the upper atmosphere from space, and while diffusing down to lower altitudes the grains will sublimate (vaporize) according to the speed and size of the grains (Moses and Poppe, 2017; Hamil et al., 2018). The grain sizes and velocities derived from the Cassini CDA instrument data

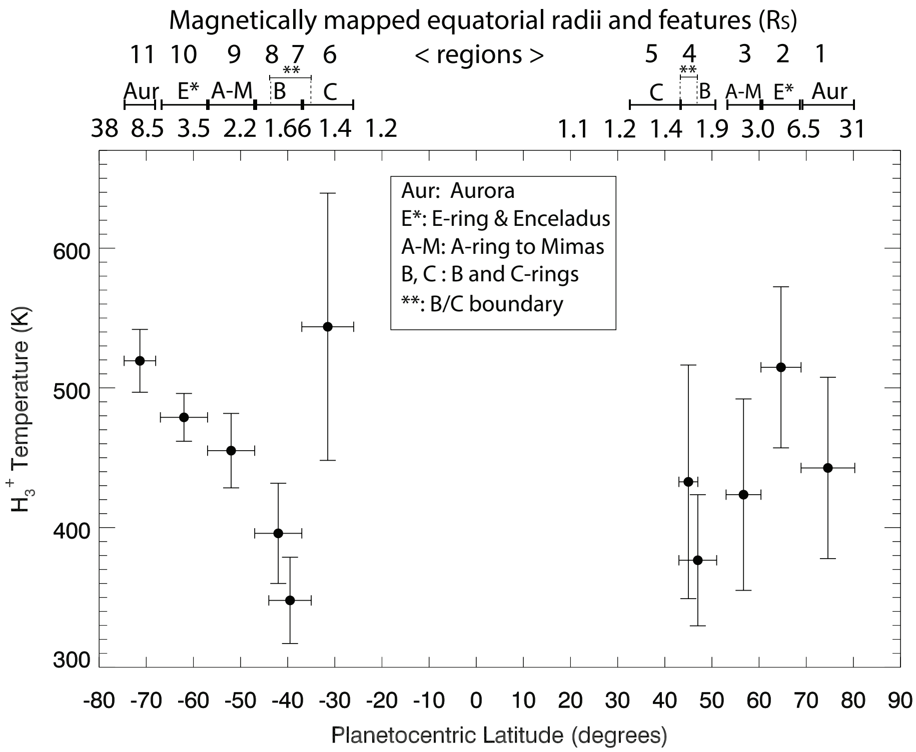

Figure 6: Saturn's fitted H_3^+ column averaged temperatures, $T_{H_3^+}$, as a function of planetocentric latitude and corresponding magnetic field mapping out to the equatorial plane, R_s. Latitudinal/radial ranges of each measurement are given by the horizontal lines on each value, while the temperature uncertainties (one standard deviation) are given by vertical lines. The listed features are the approximate locations covered by each latitudinal swath.

were generally found to be ∼10s of nm in radius and have velocities of up to several km s^{-1} (Hsu et al., 2018). According to the grain precipitation model of Hamil et al. (2018), the nearest matching grain velocity/size for grains that undergo significant sublimation are either 15 km s^{-1} / 100 nm (which disintegrate by 1085 km altitude) or 25 km s^{-1} / 10 nm (1408 km final altitude). When a photochemical model examined the release of a parcel of water in Saturn's atmosphere at 1750 km, it was found that the heaviest losses to electron densities occur by altitudes of 1000 km (Moore and Mendillo, 2007). We will assume (therefore) that chemical reactions between water products and the atmosphere are most fervent near 1000 km, following sublimation within the 1000 - 1500 km range (Moses and Poppe, 2017). With the addition of water products to lower altitudes, local electron densities would be reduced and consequently H_3^+ ions would then have longer lifetimes, while the column-integrated emissions become more representative of the deeper, colder parts of the ionosphere (Moore et al., 2009; Tao et al., 2011). The high reported temperature in the south mapping to the C-ring may then be due to lower-atmospheric H_3^+ being depleted by the aforementioned 'overflow' at lower latitudes, leaving primarily hotter/high-altitude upper-atmospheric H_3^+ to be detected. A corresponding anti-correlation between $N_{H_3^+}$ and $T_{H_3^+}$ is also be present at 45°N, although the uncertainties in the region are too large to draw any definitive conclusions.

The mid-latitude temperatures reported here are mostly a few 10s Kelvin lower in temperature than those reported for the exosphere by Koskinen et al. (2015), an offset which was predicted by Moore et al. (2015). However, at latitudes pertaining to ring rain the temperatures are far lower, likely due to the anti-correlation effect described in the previous paragraph. The auroral/polar observations reported here were also analyzed by O'Donoghue et al. (2014), who compared and contrasted Saturn's main auroral emissions in each hemisphere by summing the data between 68 - 80° north and south planetocentric latitude. Absence of Kronian-atmospheric windows (by methane absorption of sunlight) at the low latitudes led to only two H_3^+ lines being usable in the present work, whereas five H_3^+ lines were able to be used in the auroral regions of the previous study, leading to lower uncertainties. The northern H_3^+ temperature and density was found to be 527 ± 18 K and 1.6 x10^{11} ±0.3 cm^{-2}, while the southern parameters were 583 ±13 K and 1.2 x10^{11} ±0.2 cm^{-2}, respectively O'Donoghue et al. (2014). We mostly overlap these northern auroral latitudes and partially overlap the southern latitudes in this work (see Table 1), and see the same general results within uncertainties: that the southern aurorae of Saturn have hotter, less dense H_3^+ than the northern aurorae. The northern auroral temperatures (region 1) are colder at 443 ± 65 K, but this may be due to O'Donoghue et al. (2014) including 1 degree latitude more of region 2 than we do in the present paper.

The radiative cooling rate of H_3^+, $L_{H_3^+}$, is shown in Figure 7 as a function of latitude. By far the largest output of radiation to space from H_3^+ leaves from the southern auroral regions, a result that was also found at Saturn using Keck data in both 2011 and 2013 (O'Donoghue et al., 2014, 2016).

The pole-to-pole radiative cooling rate falls off towards the mid latitudes but lingers particularly high near 62°S. $L_{H_3^+}$ appears to be driven by relatively high $N_{H_3^+}$ as opposed to $T_{H_3^+}$ in this region. Region 10, around 62°S, is of special interest because a 'second auroral oval' of H_3^+ was found at this location by Stallard et al. (2008), followed by detection of the northern Enceladus footprint in the UV (Pryor et al., 2011). This region maps to the icy moon Enceladus which orbits at 3.95 R_s (Tokar et al., 2008). Enceladus is a geologically active body, outgassing neutral water products into a broad torus which encircles Saturn, some of which becomes charged by photoionization and charge-exchange (Johnson et al., 2006). A field-aligned current system between Saturn and the Enceladus torus is thought to arise from this that heats Saturn's ionosphere, owing to ionospheric drag induced by accelerating the charged part of the torus into co-rotation with the planet (Ray et al., 2012). If charged water ions from the torus are able to flow into the ionosphere, they could have also caused the subtle rise in H_3^+ density seen here in a similar manner to ring rain. It is possible that both heating and ionized water precipitation occur simultaneously, but our results hint that charged water from Enceladus may be preferentially draining into Saturn's southern mid-latitudes. It is unclear why latitudes in the northern hemisphere associated with Enceladus do not also show a large H_3^+ density.

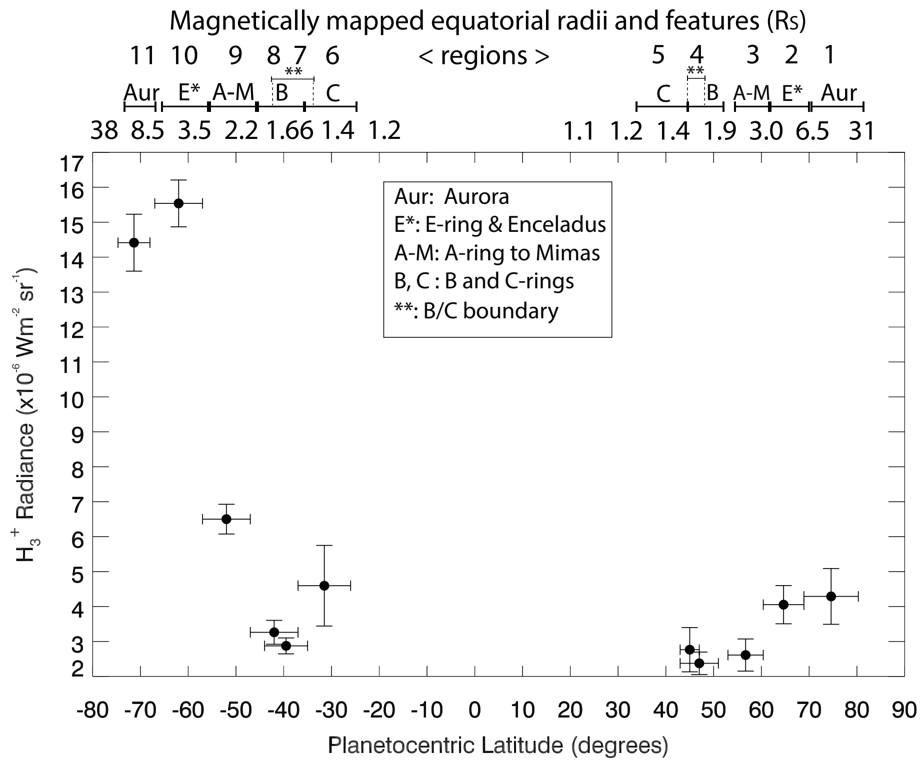

Figure 7: Saturn's fitted H_3^+ radiances (radiative cooling rates), $L_{H_3^+}$, as a function of planetocentric latitude and corresponding magnetic field mapping out to the equatorial plane, R_s. Latitudinal/radial ranges of each measurement are given by the horizontal lines on each value, while the radiance uncertainties (one standard deviation) are given by vertical lines. The listed features are the approximate locations covered by each latitudinal swath.

5. Conclusions

Ground-based observations of Saturn were obtained on 17 April 2011 using the 10-metre Keck telescope on Mauna Kea, Hawaii. H_3^+ emissions were previously analyzed from these observations, showing peaks in emission at specific latitudes that correspond well with an expected influx of charged water products (O'Donoghue et al., 2013). Subsequent modeling showed that the larger emissions are most likely driven by an increase in H_3^+ density (rather than temperature) relative to adjacent latitudes, and that this is facilitated by the removal of electrons which allow the H_3^+ lifetime to be extended where the influx occurs (Moore et al., 2015). In this study we performed a new analysis of the April 2011 data, successfully deriving the H_3^+ parameters temperature, density and radiative cooling rates for the first time at the non-auroral regions of Saturn. Until now, we have not had direct evidence that H_3^+ densities are driving the peaks in H_3^+ emission. Our findings are summarized below:

1. We find that H_3^+ density is enhanced near 45°N and 39°S planetocentric latitudes. An influx of ring material (probably water) causes the enhancements seen through the chemical pathway described by Moore et al. (2015).
2. The high H_3^+ density at 39°S is due to the northward-offset magnetic field in the vicinity of the ring plane, which leads to charged grains being immediately drawn southwards due to gravitational forces in that region (Connerney, 1986). Southern hemisphere mapping to the C-ring shows low H_3^+ density, likely due to the expected very large water influx that begins to decrease H_3^+ densities when charge-exchange between with water and H_3^+ begins to dominate (Moore et al., 2015). We define this area as an 'overflow region'.
3. We estimated the water product influx needed to explain the H_3^+ densities by using previous modeling results (Moore et al., 2015). The rates obtained were in agreement with the modeling work decades earlier by Connerney and Waite (1984).The total water influx from the rings to Saturn's mid-latitude ionosphere inferred from the H_3^+ measurements herein is 432 - 2870 kg s^{-1}, values that would deplete the rings in 292^{+818}_{-124} million years.
4. An anti-correlation between H_3^+ temperature and density was observed. H_3^+ temperatures were low while the density was high at 39°S, likely indicating that the ionosphere is most affected by ring rain in the deep ionosphere near 1200 km (Moore and Mendillo, 2007; Hamil et al., 2018), as deeper precipitation necessarily weights the H_3^+ density and emissions to colder parts of the ionosphere (Moore et al., 2009; Tao et al., 2011). In the region 6 (32° S) 'overflow region', this weighting is reversed and high-altitude, warm H_3^+ emission dominate, as low-altitude H_3^+ is expected to be completely depleted.
5. Saturn's icy moon Enceladus appears to affect the mid-latitudes, with 62°S exhibiting relatively high H_3^+ density compared to adjacent latitudes. The results may indicate that charged water from Enceladus is draining into Saturn's southern mid-latitudes, though no corresponding

northern density peak was found.

Acknowledgements James O'Donoghue's research was supported by an appointment to the National Aeronautics and Space Administration (NASA) Postdoctoral Program at the NASA Goddard Space Flight Center, administered by Universities Space Research Association under contract with NASA. This material is based upon work supported by NASA under Grants NNX14AG72G and NNX17AF14G issued through the SSO Planetary Astronomy Program. The data presented herein were obtained at the W.M. Keck Observatory, which is Operated as a scientific partnership among the California Institute of Technology, the University of California, and NASA, and the data in the form of fits files are available from the Keck archive at https://www2.keck.hawaii.edu/koa/public/koa.php We are grateful to the staff at the Keck Observatory. The authors wish to recognize the significant cultural role and reverence that the summit of Maunakea has within the indigenous Hawaiian community: we are fortunate to have the opportunity to conduct observations from this mountain.

Atreya, S. K., Donahue, T. M., Nagy, A. F., Waite, Jr., J. H., McConnell, J. C., 1984. Theory, measurements, and models of the upper atmosphere and ionosphere of Saturn. University of Arizona Press, pp. 239–277.

Connerney, J., Apr. 2013. Solar system: Saturn's ring rain. Nature 496, 178–179.

Connerney, J. E. P., Aug. 1986. Magnetic connection for Saturn's rings and atmosphere. Geophys. Res. Lett. 13, 773–776.

Connerney, J. E. P., Ness, N. F., Acuna, M. H., Jul. 1982. Zonal harmonic model of Saturn's magnetic field from Voyager 1 and 2 observations. Nature 298, 44–46.

Connerney, J. E. P., Waite, J. H., Nov. 1984. New model of Saturn's ionosphere with an influx of water from the rings. Nature 312, 136–138.

Cuzzi, J., Clark, R., Filacchione, G., French, R., Johnson, R., Marouf, E., Spilker, L., 2009. Ring Particle Composition and Size Distribution. Springer, Dordrecht, p. 459.

Cuzzi, J. N., French, R. G., Hendrix, A. R., Olson, D. M., Roush, T., Vahidinia, S., Jul. 2018. HST-STIS spectra and the redness of Saturn's rings. Icarus 309, 363–388.

Dougherty, M. K., Achilleos, N., Andre, N., Arridge, C. S., Balogh, A., Bertucci, C., Burton, M. E., Cowley, S. W. H., Erdos, G., Giampieri, G., Glassmeier, K.-H., Khurana, K. K., Leisner, J., Neubauer, F. M., Russell, C. T., Smith, E. J., Southwood, D. J., Tsurutani, B. T., Feb. 2005. Cassini Magnetometer Observations During Saturn Orbit Insertion. Science 307, 1266–1270.

Dougherty, M. K., Cao, H., Khurana, K. K., Hunt, G. J., Provan, G., Kellock, S., Burton, M. E., Burk, T. A., Bunce, E. J., Cowley, S. W. H., Kivelson, M. G., Russell, C. T., Southwood, D. J., 2018. Saturn's magnetic field revealed by the cassini grand finale. Science 362 (6410). URL `http://science.sciencemag.org/content/362/6410/eaat5434`

Dougherty, M. K., Khurana, K. K., Neubauer, F. M., Russell, C. T., Saur, J., Leisner, J. S., Burton, M. E., Mar. 2006. Identification of a Dynamic Atmosphere at Enceladus with the Cassini Magnetometer. Science 311, 1406–1409.

Hamil, O., Cravens, T. E., Reedy, N. L., Sakai, S., Feb. 2018. Fate of Ice Grains in Saturn's Ionosphere. J. Geophys. Res. (Space Physics) 123, 1429–1440.

Hansen, C. J., Shemansky, D. E., Esposito, L. W., Stewart, A. I. F., Lewis, B. R., Colwell, J. E., Hendrix, A. R., West, R. A., Waite, Jr., J. H., Teolis, B., Magee, B. A., Jun. 2011. The composition and structure of the Enceladus plume. Geophys. Res. Lett. 38, L11202.

Hsu, H.-W., Schmidt, J., Kempf, S., Postberg, F., Moragas-Klostermeyer, G., Seiß, M., Hoffmann, H., Burton, M., Ye, S., Kurth, W. S., Horányi, M., Khawaja, N., Spahn, F., Schirdewahn, D., O'Donoghue, J., Moore, L., Cuzzi, J., Jones, G. H., Srama, R., 2018. In situ collection of dust grains falling from saturn's rings into its atmosphere. Science 362 (6410). URL `http://science.sciencemag.org/content/362/6410/eaat3185`

Johnson, R. E., Melin, H., Stallard, T. S., Tao, C., Nichols, J. D., Chowdhury, M. N., Jul. 2018. Mapping H_3^+ Temperatures in Jupiter's Northern Auroral Ionosphere Using VLT-CRIRES. J. Geophys. Res. (Space Physics) 123, 5990–6008.

Johnson, R. E., Smith, H. T., Tucker, O. J., Liu, M., Burger, M. H., Sittler, E. C., Tokar, R. L., Jun. 2006. The Enceladus and OH Tori at Saturn. Astrophys. J. 644, L137–L139.

Kim, Y. H., Fox, J. L., Black, J. H., Moses, J. I., Jan. 2014. Hydrocarbon ions in the lower ionosphere of Saturn. J. Geophys. Res. (Space Physics) 119, 384–395.

Kliore, A. J., Nagy, A., Asmar, S., Anabtawi, A., Barbinis, E., Fleischman, D., Kahan, D., Klose, J., Aug. 2014. The ionosphere of Saturn as observed by the Cassini Radio Science System. Geophys. Res. Lett. 41, 5778–5782.

Kliore, A. J., Patel, I. R., Lindal, G. F., Sweetnam, D. N., Hotz, H. B., Waite, J. H., McDonough, T., Nov. 1980. Structure of the ionosphere and atmosphere of Saturn from Pioneer 11 Saturn radio occultation. J. Geophys. Res. 85, 5857–5870.

Koskinen, T. T., Sandel, B. R., Yelle, R. V., Strobel, D. F., Müller-Wodarg, I. C. F., Erwin, J. T., Nov. 2015. Saturn's variable thermosphere from Cassini/UVIS occultations. Icarus 260, 174–189.

Lam, H. A., Achilleos, N., Miller, S., Tennyson, J., Trafton, L. M., Geballe, T. R., Ballester, G. E., Jun. 1997. A Baseline Spectroscopic Study of the Infrared Auroras of Jupiter. Icarus 127, 379–393.

Liu, C.-M., Ip, W.-H., May 2014. A New Pathway of Saturnian Ring-Ionosphere Coupling via Charged Nanograins. Astrophys. J. 786, 34.

Markwardt, C. B., Sep. 2009. Non-linear Least-squares Fitting in IDL with MPFIT. In: Bohlender, D. A., Durand, D., Dowler, P. (Eds.), Astronomical Data Analysis Software and Systems XVIII. Vol. 411 of Astronomical Society of the Pacific Conference Series. p. 251.

McElroy, M. B., Mar. 1973. The Ionospheres of the Major Planets (Article published in the Space Science Reviews special issue on 'Outer Solar System Exploration - An Overview', ed. by J. E. Long and D. G. Rea.). Space Sci. Rev. 14, 460–473.

McLean, I. S., Becklin, E. E., Bendiksen, O., Brims, G., Canfield, J., Figer, D. F., Graham, J. R., Hare, J., Lacayanga, F., Larkin, J. E., Larson, S. B., Levenson, N., Magnone, N., Teplitz, H., Wong, W., Aug. 1998. Design and development of NIRSPEC: a near-infrared echelle spectrograph for the Keck II telescope. In: Fowler, A. M. (Ed.), Society of Photo-Optical Instrumentation Engineers (SPIE) Conference Series. Vol. 3354 of Society of Photo-Optical Instrumentation Engineers (SPIE) Conference Series. pp. 566–578.

Melin, H., Stallard, T. S., Miller, S., Geballe, T. R., Trafton, L. M., O'Donoghue, J., 2013. Post-equinoctial observations of the ionosphere of uranus. Icarus 223 (2), 741 – 748.

Melin, H., Stallard, T. S., O'Donoghue, J., Badman, S. V., Miller, S., Blake, J. S. D., Feb. 2014. On the anticorrelation between H_3^+ temperature and density in giant planet ionospheres. Mon. Not. R. Astron. Soc. 438, 1611–1617.

Miller, S., Stallard, T., Melin, H., Tennyson, J., 2010. H_3^+ cooling in planetary atmospheres. Faraday Discussions 147, 283–291.

Mitchell, D. G., Perry, M. E., Hamilton, D. C., Westlake, J. H., Kollmann, P., Smith, H. T., Carbary, J. F., Waite, J. H., Perryman, R., Hsu, H.-W., Wahlund, J.-E., Morooka, M. W., Hadid, L. Z., Persoon, A. M., Kurth, W. S., 2018. Dust grains fall from saturn's d-ring into its equatorial upper atmosphere. Science 362 (6410).
URL http://science.sciencemag.org/content/362/6410/eaat2236

Moore, L., Galand, M., Mueller-Wodarg, I., Mendillo, M., Dec. 2009. Response of Saturn's ionosphere to solar radiation: Testing parameterizations for thermal electron heating and secondary ionization processes. Planetary and Space Science 57, 1699–1705.

Moore, L., Mendillo, M., Jun. 2007. Are plasma depletions in Saturn's ionosphere a signature of time-dependent water input? Geophys. Res. Lett. 34, 12202.

Moore, L., O'Donoghue, J., Müller-Wodarg, I., Galand, M., Mendillo, M., Jan. 2015. Saturn ring rain: Model estimates of water influx into Saturn's atmosphere. Icarus 245, 355–366.

Moses, J. I., Bass, S. F., Mar. 2000. The effects of external material on the chemistry and structure of Saturn's ionosphere. J. Geophys. Res. 105, 7013–7052.

Moses, J. I., Poppe, A. R., Nov. 2017. Dust ablation on the giant planets: Consequences for stratospheric photochemistry. Icarus 297, 33–58.

Neale, L., Miller, S., Tennyson, J., Jun. 1996. Spectroscopic Properties of the H_3^+ Molecule: A New Calculated Line List. Astrophys. J. 464, 516–520.

Nicholson, P. D., Hedman, M. M., Clark, R. N., Showalter, M. R., Cruikshank, D. P., Cuzzi, J. N., Filacchione, G., Capaccioni, F., Cerroni, P., Hansen, G. B., Sicardy, B., Drossart, P., Brown, R. H., Buratti, B. J., Baines, K. H., Coradini, A., Jan. 2008. A close look at Saturn's rings with Cassini VIMS. Icarus 193, 182–212.

Northrop, T. G., Connerney, J. E. P., Apr. 1987. A micrometeorite erosion model and the age of Saturn's rings. Icarus 70, 124–137.

Northrop, T. G., Hill, J. R., Aug. 1982. Stability of negatively charged dust grains in Saturn's ring plane. J. Geophys. Res. 87, 6045–6051.

Northrop, T. G., Hill, J. R., Aug. 1983. The inner edge of Saturn's B ring. J. Geophys. Res. 88, 6102–6108.

O'Donoghue, J., Melin, H., Stallard, T. S., Provan, G., Moore, L., Badman, S. V., Cowley, S. W. H., Baines, K. H., Miller, S., Blake, J. S. D., Jan. 2016. Ground-based observations of Saturn's auroral ionosphere over three days: Trends in ${H_3}^+$ temperature, density and emission with Saturn local time and planetary period oscillation. Icarus 263, 44–55.

O'Donoghue, J., Moore, L., Connerney, J. E. P., Melin, H., Stallard, T. S., Miller, S., Baines, K. H., Dec. 2017. Redetection of the Ionospheric H3+ Signature of Saturn's "Ring Rain". Geophys. Res. Lett. 44, 11.

O'Donoghue, J., Stallard, T. S., Melin, H., Cowley, S. W. H., Badman, S. V., Moore, L., Miller, S., Tao, C., Baines, K. H., Blake, J. S. D., Feb. 2014. Conjugate observations of Saturn's northern and southern H_3^+ aurorae. Icarus 229, 214–220.

O'Donoghue, J., Stallard, T. S., Melin, H., Jones, G. H., Cowley, S. W. H., Miller, S., Baines, K. H., Blake, J. S. D., Apr. 2013. The domination of Saturn's low-latitude ionosphere by ring 'rain'. Nature 496, 193–195.

Perry, M., Waite Jr, J., Mitchell, D., Miller, K., Cravens, T., Perryman, R., Moore, L., Yelle, R., Hsu, H.-W., Hedman, M., et al., 2018. Material flux from the rings of saturn into its atmosphere. Geophys. Res. Lett.

Prangé, R., Fouchet, T., Courtin, R., Connerney, J. E. P., McConnell, J. C., Feb. 2006. Latitudinal variation of Saturn photochemistry deduced from spatially-resolved ultraviolet spectra. Icarus 180, 379–392.

Pryor, W. R., Rymer, A. M., Mitchell, D. G., Hill, T. W., Young, D. T., Saur, J., Jones, G. H., Jacobsen, S., Cowley, S. W. H., Mauk, B. H., Coates, A. J., Gustin, J., Grodent, D., Gérard, J.-C., Lamy, L., Nichols, J. D., Krimigis, S. M., Esposito, L. W., Dougherty, M. K., Jouchoux, A. J., Stewart, A. I. F., McClintock, W. E., Holsclaw, G. M., Ajello, J. M., Colwell, J. E., Hendrix, A. R., Crary, F. J., Clarke, J. T., Zhou, X., Apr. 2011. The auroral footprint of Enceladus on Saturn. Nature 472, 331–333.

Ray, L. C., Galand, M., Moore, L. E., Fleshman, B. L., Jul. 2012. Characterizing the limitations to the coupling between Saturn's ionosphere and middle magnetosphere. J. Geophys. Res. (Space Physics) 117, A07210.

Srama, R., Ahrens, T. J., Altobelli, N., Auer, S., Bradley, J. G., Burton, M., Dikarev, V. V., Economou, T., Fechtig, H., Görlich, M., Grande, M., Graps, A., Grün, E., Havnes, O., Helfert, S., Horanyi, M., Igenbergs, E., Jessberger, E. K., Johnson, T. V., Kempf, S., Krivov, A. V., Krüger, H., Mocker-Ahlreep, A., Moragas-Klostermeyer, G., Lamy, P., Landgraf, M., Linkert, D., Linkert, G., Lura, F., McDonnell, J. A. M., Möhlmann, D., Morfill, G. E., Müller, M., Roy, M., Schäfer, G., Schlotzhauer, G., Schwehm, G. H., Spahn, F., Stübig, M., Svestka, J., Tschernjawski, V., Tuzzolino, A. J., Wäsch, R., Zook, H. A., Sep. 2004. The Cassini Cosmic Dust Analyzer. Space Sci. Rev. 114, 465–518.

Stallard, T., Miller, S., Melin, H., Lystrup, M., Cowley, S. W. H., Bunce, E. J., Achilleos, N., Dougherty, M., Jun. 2008. Jovian-like aurorae on Saturn. Nature 453, 1083–1085.

Stallard, T. S., Melin, H., Miller, S., Badman, S. V., Baines, K. H., Brown, R. H., Blake, J. S. D., O'Donoghue, J., Johnson, R. E., Bools, B., Pilkington, N. M., East, O. T. L., Fletcher, M., Aug. 2015. Cassini VIMS observations of H_3^+ emission on the nightside of Jupiter. J. Geophys. Res. (Space Physics) 120, 6948–6973.

Stallard, T. S., Melin, H., Miller, S., O' Donoghue, J., Cowley, S. W. H., Badman, S., Adriani, A., Brown, R. H., Baines, K. H., Oct. 2012. Temperature changes and energy inputs in giant planet atmospheres: what we are learning from H_3^+. Phil. Trans. Roy. Soc. 370, 5213–5224.

Tao, C., Badman, S. V., Fujimoto, M., Jun. 2011. UV and IR auroral emission model for the outer planets: Jupiter and Saturn comparison. Icarus 213, 581–592.

Tokar, R. L., Wilson, R. J., Johnson, R. E., Henderson, M. G., Thomsen, M. F., Cowee, M. M., Sittler, E. C., Young, D. T., Crary, F. J., McAndrews, H. J., Smith, H. T., Jul. 2008. Cassini detection of water-group pick-up ions in the Enceladus torus. Geophys. Res. Lett. 35, 14202.

Voosen, P., Dec. 2017. Saturn's rings are solar system newcomers. Science 358, 1513–1514.

Waite, J. H., Atreya, S. K., Nagy, A. F., Sep. 1979. The ionosphere of Saturn - Predictions for Pioneer 11. Geophys. Res. Lett. 6, 723–726.

Waite, J. H., Perryman, R. S., Perry, M. E., Miller, K. E., Bell, J., Cravens, T. E., Glein, C. R., Grimes, J., Hedman, M., Cuzzi, J., Brockwell, T., Teolis, B., Moore, L., Mitchell, D. G., Persoon, A., Kurth, W. S., Wahlund, J.-E., Morooka, M., Hadid, L. Z., Chocron, S., Walker, J., Nagy, A., Yelle, R., Ledvina, S., Johnson, R., Tseng, W., Tucker, O. J., Ip, W.-H., 2018. Chemical interactions between saturn's atmosphere and its rings. Science 362 (6410).
URL http://science.sciencemag.org/content/362/6410/eaat2382

Zebker, H. A., Marouf, E. A., Tyler, G. L., Dec. 1985. Saturn's rings - Particle size distributions for thin layer model. Icarus 64, 531–548.